

## ELECTRONIC SUPPLEMENTARY INFORMATION (ESI)

### **Shape Effect in Cellular Uptake of PEGylated Nanoparticles: Comparison between sphere, rod, cube and disk**

#### **Ying Li**

Department of Mechanical Engineering, Northwestern University, Evanston, IL, USA

E-mail: [yingli@u.northwestern.edu](mailto:yingli@u.northwestern.edu)

#### **Martin Kröger**

Polymer Physics, Department of Materials, ETH Zurich, 8093 Zurich, Switzerland

E-mail: [mk@mat.ethz.ch](mailto:mk@mat.ethz.ch)

#### **Wing Kam Liu**

Department of Mechanical Engineering, Northwestern University, Evanston, IL, USA

Adjunct Professor under the Distinguished Scientists Program Committee at King Abdulaziz University (KAU), Jeddah, Saudi Arabia

E-mail: [w-liu@northwestern.edu](mailto:w-liu@northwestern.edu)

## 1. Model and methodology

### 1.1. DPD method

Dissipative particle dynamics (DPD) method is a coarse-grained simulation technique, which can correctly account for the hydrodynamic interactions by considering water molecules explicitly [1–3]. In the DPD simulation, each bead with mass  $m$  represents a group of atoms or molecules. Beads  $i$  and  $j$  interact with each other through a pairwise additive force with three major contributions: (i) a conservative force  $\mathbf{F}_{ij}^C$ ; (ii) a dissipative force  $\mathbf{F}_{ij}^D$ ; and (iii) a random force  $\mathbf{F}_{ij}^R$ . Therefore, the force applied on atom  $i$  due to atom  $j$  is given as a sum of these three terms:

$$\mathbf{F}_i = \mathbf{F}_{ij}^C + \mathbf{F}_{ij}^D + \mathbf{F}_{ij}^R, \quad r_{ij} < r_c \quad (1)$$

where  $r_{ij}$  is the distance between beads  $i$  and  $j$ ;  $r_c$  is the cutoff distance. The conservative force is  $\mathbf{F}_{ij}^C = a_{ij}\omega(r_{ij})\hat{\mathbf{r}}_{ij}$ , where  $a_{ij}$  is the maximum repulsive force and  $\hat{\mathbf{r}}_{ij} = \mathbf{r}_{ij}/r_{ij}$  is the unit vector. The weight  $\omega(r_{ij})$  is a normalized distribution function, defined as

$$\omega(r_{ij}) = \begin{cases} 1 - r_{ij}/r_c, & r_{ij} \leq r_c, \\ 0, & r_{ij} > r_c. \end{cases} \quad (2)$$

Dissipative force  $\mathbf{F}_{ij}^D = -\gamma\omega^2(r_{ij})(\hat{\mathbf{r}}_{ij}\dot{v}_{ij})\hat{\mathbf{r}}_{ij}$ , with  $v_{ij}$  representing the relative velocity between beads  $i$  and  $j$ . Random force  $\mathbf{F}_{ij}^R = \sigma\omega(r_{ij})\alpha\delta t^{-1/2}\hat{\mathbf{r}}_{ij}$ .  $\alpha$  is a Gaussian random number with zero mean and unit variance.  $\delta t$  is the time step. The parameters  $\gamma$  and  $\sigma$  are related to each other as  $\sigma^2 = 2\gamma k_B T$ , where  $k_B$  and  $T$  are the Boltzmann's constant and temperature, respectively.

In our DPD simulation, the mass, length, and time scale are all normalized. The unit of length is taken to be the cutoff radius  $r_c$ . The unit of mass is that of the solvent beads. The unit of energy is taken to be  $k_B T$ . Then, all other quantities are given in terms of these basic units. In terms of normalized units, we use the standard values for  $\sigma$  and  $\gamma$  as  $\sigma = 3.0$  and  $\gamma = 4.5$ . The reduced DPD units can be easily converted into the SI units by mapping the membrane thickness and lipid diffusion coefficient from DPD simulation results to experimental measured values. In our DPD simulations, the velocity-Verlet integration algorithm is adopted and the simulation time step is  $\delta t = 0.01\tau$  with  $\tau = [mr_c^2/(k_B T)]^{1/2}$ .

### 1.2. DPD model for lipid bilayer

Similar to the lipid model developed by Groot and Rabone [4], the lipid is represented by the  $H_3(T_5)_2$  model. The head of lipid molecule is formed by three hydrophilic beads (H), while each of the tails is formed by five hydrophobic beads (T). The head and tail beads are colored by iceblue and silver, respectively. The neighboring beads  $i$  and  $j$  in the lipid are connected together by a simple harmonic spring:

$$U_s = k_s(1 - r_{ij}/r_s)^2, \quad (3)$$

where spring constant  $k_s = 50k_B T/r_c^2$  and equilibrium bond length  $r_s = 0.7r_c$  [4]. To ensure the linearity of the lipid head as well as its tail, a harmonic constraint is applied on the adjacent three beads,

$$U_b = k_b(\theta - \theta_0)^2, \quad (4)$$

where  $k_b$ ,  $\theta$  and  $\theta_0$  are the bending constant, the inclination angle, and equilibrium angle value, respectively. Following the work done by Groot and Rabone [4],  $k_1 = 3.0k_B T/r_c^2$  and  $\theta_0 = 180^\circ$  for the three consecutive lipid head/tail beads in the lipid molecules. However, for the head bead connected to the first beads in the two tails,  $k_2 = 1.5k_B T/r_c^2$  and  $\theta_0 = 120^\circ$ . For the two consecutive head beads connected to the first bead in each tail, we have  $k_3 = 2.25k_B T/r_c^2$  and  $\theta_0 = 120^\circ$ . To represent the hydrophilic/hydrophobic property of the head and tail beads in the lipid molecule, the repulsive interaction parameters for the same type of beads are  $a_{ij} = 25$ . The interaction parameters for lipid head/tail with solvent (water) molecules are  $a_{HT} = a_{ST} = 100$  and  $a_{HS} = a_{SS} = 25$ . Here H, T and S represent the lipid head, tail and solvent (water) beads in the DPD model.

The simulation box for studying PEGylated NPs is a cube of size  $51.2 \times 51.2 \times 51.2 r_c$ , with periodic boundary condition applied along  $x$ ,  $y$  and  $z$  directions. There are 2,888 lipid molecules (37,544 beads in total) with 396,566 solvent beads. Therefore, the particle density is close to 3.0. For clarity, the solvent beads are not shown in the figures. The area per lipid is about  $1.81r_c^2$ , which ensures the zero surface tension of the lipid bilayer [4–6]. The simulated lipid bilayer thickness is about  $5r_c$ . By comparing with the experimentally measured thickness for 1-palmitoyl-2-oleoyl-sn-glycero-3-phosphocholine (POPC) bilayer, which is about 4 nm [7], the basic length unit in the DPD simulation is about  $r_c \sim 0.8$  nm. By mapping the diffusion coefficient around  $5 \mu\text{m}^2/\text{s}$  for POPC bilayer [7], the time unit in the DPD simulation is about  $\tau = 24.32$  ps.

### 1.3. DPD model for polyethylene glycol

Polyethylene glycol (PEG) is a hydrophilic polymer with chemical structure  $\text{H}-(\text{O}-\text{CH}_2-\text{CH}_2)_n-\text{OH}$ , which is also known as the polyethylene oxide (PEO) or polyoxyethylene (POE), depending on its molecule weight. To efficiently model the PEG polymer in our DPD simulations, we adopt the coarse-grained model for PEG developed by Lee *et al* [8]. In this model, each ethylene oxide ( $\text{O}-\text{CH}_2-\text{CH}_2$ ) group has been coarse-grained into one bead. The neighboring beads on each PEG chain are connected by a harmonic bond

$$U_{\text{bond}} = K_b(b - b_0)^2, \quad (5)$$

where  $K_b$  is the bond potential constant,  $b$  and  $b_0$  are the instantaneous and equilibrium bond lengths between PEG monomers, respectively. Here  $K_b = 8500 \text{ kJ mol}^{-1} \text{ nm}^{-2}$  and  $b_0 = 0.33 \text{ nm}$ . The angle potential formed by a triplet is described by

$$U_{\text{angle}} = K_\theta(\cos \theta - \cos \theta_0)^2, \quad (6)$$

where  $K_\theta$  is the angle potential constant,  $\theta$  and  $\theta_0$  are the instantaneous and equilibrium angles formed by two consecutive bonds, respectively.  $K_\theta = 42.5 \text{ kJ mol}^{-1}$  and  $\theta_0 = 130^\circ$ .

**Table S1.** Interaction parameters between beads  $i$  and  $j$ ,  $a_{ij}$ . S, H, T, E and P represent the solvent, lipid head, lipid tail, PEG and NP beads, respectively.  $a_{ij} - a_{ii} = 3.27\chi_{ij}$ , where  $\chi_{ij}$  is the Flory-Huggins parameter. The Flory-Huggins parameters between PEG (E), lipid head (H) and lipid tails (T) beads are taken from the work done by Groot and Rabone [4], calibrated by experimental studies.

$a_{ij}$	S	H	T	E	P
S	25.0	25.0	100.0	26.3	100.0
H	25.0	25.0	100.0	26.3	100.0
T	100.0	100.0	25.0	33.7	50.0
E	26.3	26.3	33.7	25.0	100.0
P	100.0	100.0	50.0	100.0	25.0

In the previous work done by Lee *et al* [8], the pair interactions are described by the classical Lennard-Jones 6-12 potential. However, in the DPD simulation, the pair interactions are represented by the conservative force  $\mathbf{F}_{ij}^C$  with strength of repulsion parameter  $a_{ij}$ . According to the previous experimental [9] and computational [4] studies, we set  $a_{ES} = 26.3$  and  $a_{EE} = 25$ . Here the subscripts E and S denote the ethylene oxide and solvent, respectively. The repulsive parameters  $a_{ij}$  between different beads in our DPD simulations are summarized in Table S1.

To validate and verify the PEG model adopted in our DPD simulation, we have studied the radius of gyration ( $R_g$ ) and end-to-end distance ( $R_{ee}$ ) of PEG with different chain lengths  $N$ . The simulation box of size  $30 \times 30 \times 30 r_c$  with periodical boundary conditions applied along  $x$ ,  $y$  and  $z$  directions. A single PEG chain with length  $N \in [9, 76]$  is inserted into the simulation box. Then, the additional solvent beads are added into the simulation box to satisfy the particle density 3.0. The system has been firstly equilibrated around 2 million time steps. Then, the coordinates of PEG chain have been saved every 2000 time steps in another 2 million time step simulation. As discussed in our previous study [10], the  $R_g$  and  $R_{ee}$  predicted by our DPD simulations are in good agreement with the values obtained from all-atom and coarse-grained (CG) simulations, reported by Lee *et al* [8].

## 2. Conformation of PEGylated nanoparticles (NPs)

With the given interaction parameters described in above sections and our previous work [10], all the PEGylated NPs have been well-equilibrated within water. The equilibrated configurations for PEGylated NPs are given in Figs. S1-S4. When the grafting density is low (such as 0.2 chains/nm<sup>2</sup>), the grafted PEG are far away from each other and isolated. They are collapsed on the surfaces of NPs to form a ‘mushroom’ conformation to minimize the entropy loss. However, if the grafting density is high (such as 1.6 chains/nm<sup>2</sup>), the grafted PEG chains are very close to each other. To reduce the interaction energy between them, the tethered PEG are stretched away from the surface and form a ‘brush’ conformation.

The conformation of the grafted polymer chains at a solid surface has been theoretical

studied by Szleifer and co-workers [11–13] in molecular detail. Qualitatively similar conclusions are obtained using the SCF approaches [14, 15]. When the grafting density is small and the surface is repulsive for the monomers of tethered chains, the grafted polymers are isolated. They are collapsed on the surface to reduce the conformational entropy loss. Such a conformation is so-called ‘mushroom’ regime. However, when the grafting density is very large, the tethered chains have to stretch out of the surface to minimize the steric (intermolecular) interactions, by forming the ‘brush’ regime. In the range of molecular weights adopted in biocompatible materials and drug carriers, the conformation of tethered PEG polymers gradually change from ‘mushroom’ to ‘brush’ conformations, without a sharp boundary. Such a phenomenon has been confirmed by our molecular simulations for PEGylated NPs with different shapes (cf. Figs. S1-S4).

The geometric parameters for the studied NP cores are:

$$\begin{aligned}
 \mathcal{R}_{\text{sphere}} &= 4 \text{ nm}, \\
 \mathcal{R}_{\text{disk}} &= 5.66 \text{ nm}, \\
 \mathcal{L}_{\text{cube}} &= 5.79 \text{ nm}, \\
 \mathcal{R}_{\text{rod}} &= 2.31 \text{ nm}, \quad \mathcal{L}_{\text{rod}} = 9.23 \text{ nm}.
 \end{aligned}
 \tag{7}$$

They are compatible with a NP surface area  $A_{\text{surf}} = 201 \text{ nm}^2$  for all geometries. Throughout the number of PEG monomers per chain is  $N_p = 30$ , corresponding to molecular weight 1358 Da. With  $V(R)$ , supplemented by indices that characterize the NP core shape and its dimensions, we denote the volume of the PEGylated NP with homogeneous brush height  $R$ .  $V_0(R) = V(R)/M$  stands for the mean volume per chain, where  $M = A_{\text{surf}}\sigma_p$  denotes the number of chains tethered onto a single NP. Grafting densities are varied as  $\sigma_p = 0.2, 0.4, \dots, 1.6 \text{ chains/nm}^2$ .

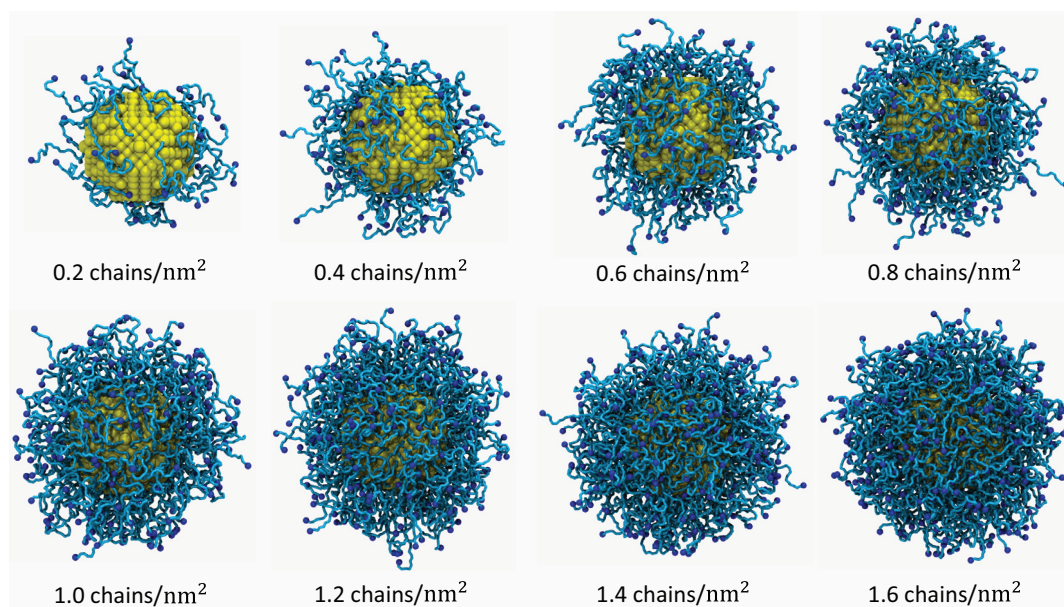


**Figure S1.** Spherical NP core. Models for PEGylated NPs with grafted PEG chains for various surface densities. The core beads are colored by yellow. The grafted PEG chains and targeting moieties bound to their free ends are colored by cyan and blue, respectively. For clarity, the solvent molecules are made invisible.

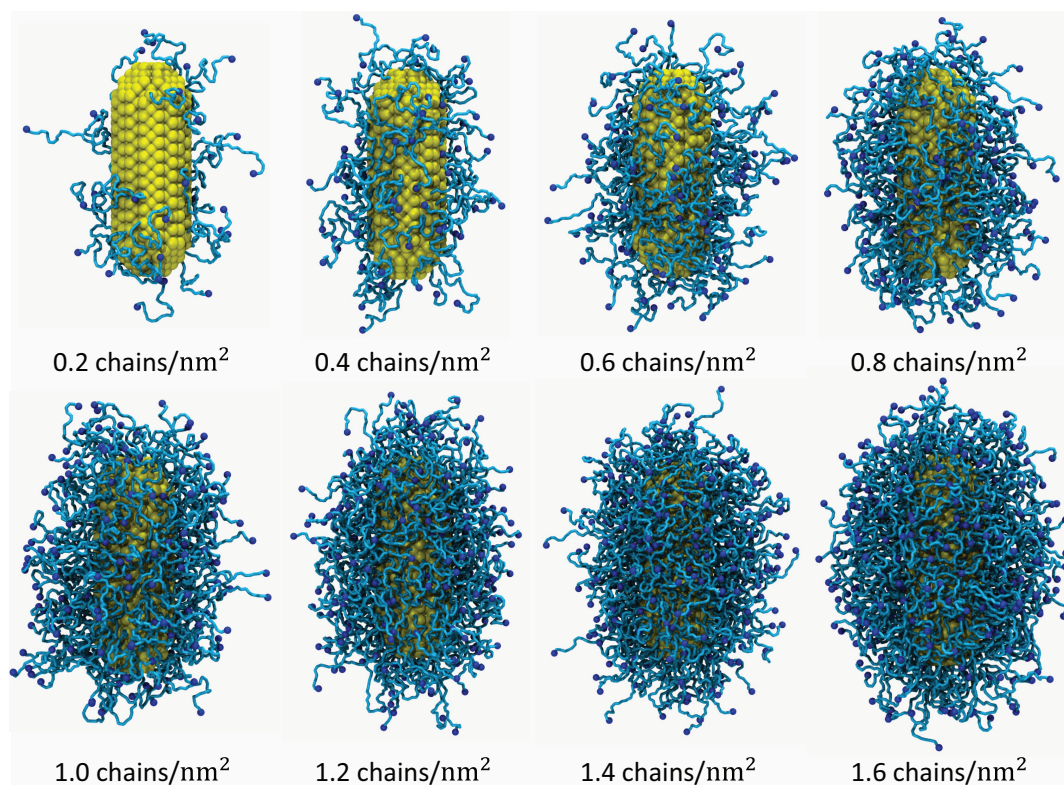


**Figure S2.** Same as Fig. S1 for the rodlike NP.

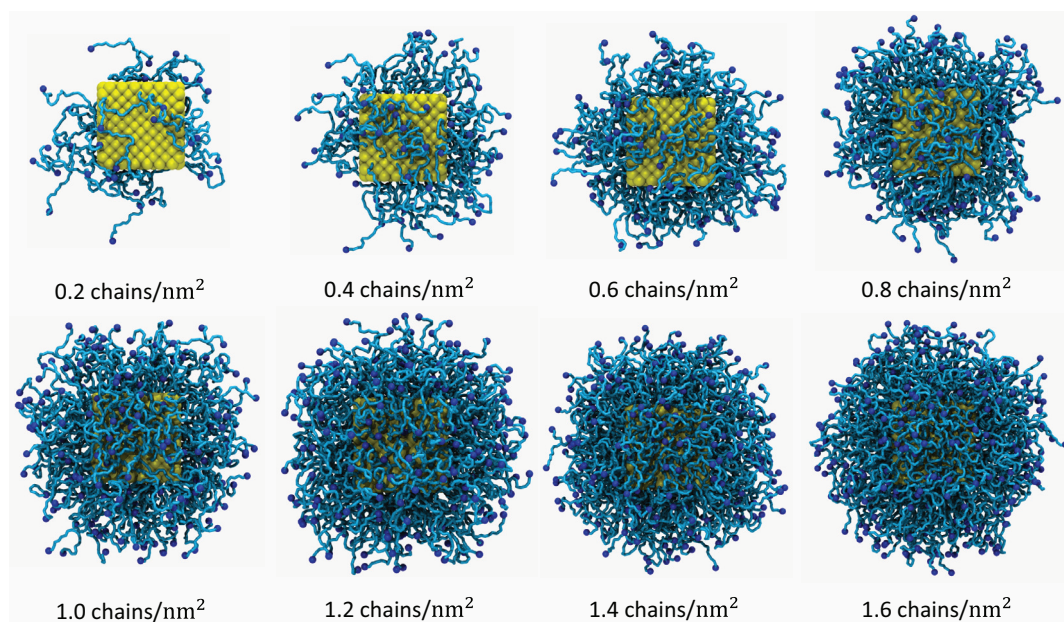


**Figure S3.** Same as Fig. S1 for the cubic NP.

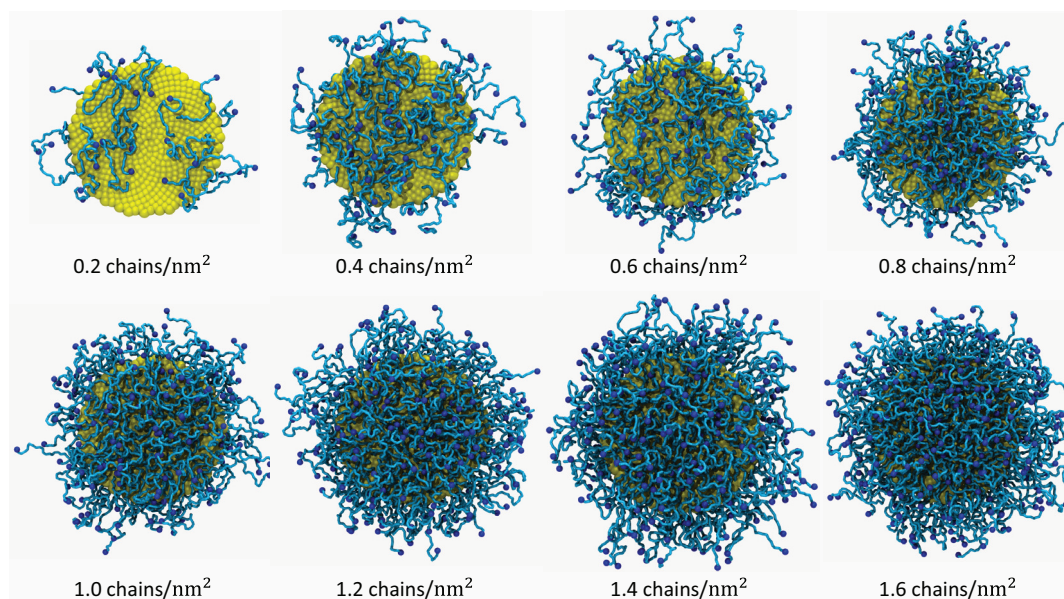


**Figure S4.** Same as Fig. S1 for the disk-like NP.

### 3. Areas and volumes; Flory theory for tethered chains

How can we understand why the extensions are of similar magnitude for the chosen setups, while it is well known that curvature effects play a major role for the extension of a polymer brush? Consider sphere and rod with hemispherical end caps, at same  $N_p$ , same number of chains  $M$ , and same grafting density  $\sigma_p$ . The volumes of assumed homogeneous polymer coatings of thickness  $R$  are

$$V_{\mathcal{R}}^{\text{sphere}}(R) = (4\pi/3)[(\mathcal{R} + R)^3 - \mathcal{R}^3], \quad (8)$$

$$V_{\mathcal{R},\mathcal{L}}^{\text{rod}}(R) = \pi[(\mathcal{R} + R)^2 - \mathcal{R}^2]\mathcal{L} + V_{\mathcal{R}}^{\text{sphere}}(R) \quad (9)$$

for a sphere of radius  $\mathcal{R}$ , and a rod of length  $\mathcal{L}$  with hemispherical end caps of radius  $\mathcal{R}$ . Tethering surface areas

$$A_{\mathcal{R}}^{\text{sphere}} = 4\pi\mathcal{R}^2, \quad (10)$$

$$A_{\mathcal{R},\mathcal{L}}^{\text{rod}} = 2\pi\mathcal{R}\mathcal{L} + A_{\mathcal{R}}^{\text{sphere}} \quad (11)$$

The requirement of identical surface areas  $A_{\text{surf}} = A_{\mathcal{R}}^{\text{sphere}} = A_{\mathcal{R},\mathcal{L}}^{\text{rod}}$  implies  $\mathcal{L}_{\text{rod}} = 2(\mathcal{R}_{\text{sphere}}^2 - \mathcal{R}_{\text{rod}}^2)/\mathcal{R}_{\text{rod}}$ . The grafting density is  $\sigma_p = M/A_{\text{surf}}$ , where  $M$  denotes the number of tethered chains. We can thus replace  $\mathcal{R}_{\text{sphere}}$  by  $(M/4\pi\sigma_p)^{1/2}$  and are left with variable  $\mathcal{R}_{\text{rod}}$ . For small  $R \ll \mathcal{R}_{\text{rod}}$  and  $R \ll \mathcal{R}_{\text{sphere}}$  the volume is  $A_{\text{surf}}R$  in either case, as for a planar setup. For huge  $R$ ,  $V_{\mathcal{R}}^{\text{sphere}}(R) = V_{\mathcal{R}}^{\text{rod}}(R) \sim R^3$ , due to the end caps. Only in intermediate regimes both  $V_{\mathcal{R}}^{\text{rod}}(R)$  and  $V_{\mathcal{R}}^{\text{sphere}}(R)$  tend to scale with  $R^2$ . If we expand both volumes in a Taylor series about  $R = 0$ , up to  $O(R^3)$  we find the corresponding coefficients

$$\frac{V_{\mathcal{R}}^{\text{sphere}}(R) - A_{\text{surf}}R}{\sqrt{A_{\text{surf}}}R^2} = 2\sqrt{\pi} \approx 3.54, \quad (12)$$

$$\frac{V_{\mathcal{R},\mathcal{L}}^{\text{rod}}(R) - A_{\text{surf}}R}{\sqrt{A_{\text{surf}}}R^2} = (1 + \rho)\sqrt{\pi/\rho} \approx 4.09 \quad (13)$$

that are seen to be insensitive to the choice of  $\mathcal{R}$ , but depend on the axis ratio of the rod,  $\rho = (\mathcal{L}_{\text{rod}} + 2\mathcal{R}_{\text{rod}})/2\mathcal{R}_{\text{rod}}$ ;  $\rho = 3$  in our simulations. Because the two numbers in Eq. 12 are not very different for our chosen setup, the extension of the brush is expected to be very comparable for all grafting densities, if we compare spherical with rodlike geometries. The sphere should tend to have a slightly larger extension due to its smaller volume,  $V_{\mathcal{R}}^{\text{sphere}}(R) < V_{\mathcal{R}}^{\text{rod}}(R)$  for all  $R$ , as long as  $\rho$  exceeds 2.54. We can do analogous calculations for cubes and disks using

$$V_{\mathcal{L}}^{\text{cube}}(R) = 6R\mathcal{L}^2 + 4\pi R^3/3 + 3\pi\mathcal{L}R^2, \quad (14)$$

$$V_{\mathcal{R}}^{\text{disk}}(R) = \pi R(4R^2 + 3\pi\mathcal{R}R + 6\mathcal{R}^2)/3 \quad (15)$$

while  $A_{\mathcal{L}}^{\text{cube}} = 6\mathcal{L}^2$  and  $A_{\mathcal{R}}^{\text{disk}} = 2\pi\mathcal{R}^2$ . The result is, up to order  $O(R^3)$ ,

$$\frac{V_{\mathcal{L}}^{\text{cube}}(R) - A_{\text{surf}}R}{\sqrt{A_{\text{surf}}}R^2} = \sqrt{3\pi^2/2} \approx 3.94, \quad (16)$$

$$\frac{V_{\mathcal{R}}^{\text{disk}}(R) - A_{\text{surf}}R}{\sqrt{A_{\text{surf}}}R^2} = \sqrt{\pi^3/2} \approx 3.85 \quad (17)$$

Again, the coefficients in front of the terms proportional to  $R^2$  and of relevance in an intermediate regime of layer thicknesses are comparable in magnitude.

This idealized consideration assumed that the polymer is homogeneously occupying a layer of constant thickness  $R$  surrounding the NP. A more precise calculation would consider only the ‘reachable’ volume, starting from an array of tethering points distributed over the NP surface. This revised volume will be smaller and exhibit more pronounced geometry effects especially when  $R$  is small compared to the linear dimensions of the NP.

As discussed in the main text we can estimate the free energy of the coated NP before endocytosis not only via SCF but also using a simple Flory approach. This paragraph aims at exemplifying on how to obtain scaling laws that help to estimate the overall trends upon changing systems parameters, while a numerical implementation is trivial as well. Within this approach the free energy per chain is

$$\frac{F_{\text{poly}}(R)}{k_{\text{B}}T} = \frac{3\zeta}{2} \left( \frac{R^2}{R_0^2} + \frac{R_0^2}{R^2} \right) + N_p \frac{vf_m(\phi_0)}{\phi_0} \quad (18)$$

with mixing free energy density  $vf_m(\phi) = \tau\phi^2 + w\phi^3$  and unconfined end-to-end distance  $R_0 \approx 0.57\sqrt{N_p}$  nm for PEG following our previous works [10]. Here  $\phi_0 = \phi_0(R) = N_p v/V_0(R)$  stands for the yet unknown mean polymer volume fraction within the coating,  $V_0(R) = V(R)/A_{\text{surf}}\sigma_p$  is the accessible volume per single chain, where the total volume of the  $R$ -coated NP,  $V(R)$ , and the surface area of the naked NP,  $A_{\text{surf}}$ , were given above for the various geometries;  $\zeta$  is a constant of order unity, and  $v \approx 0.0633$  nm<sup>3</sup> is the excluded volume of each of the  $N_p$  PEG monomers per chain.

For the special case of good solvent conditions,  $w = 0$ ,  $R \gg R_0$  and Eq. 18 reduces to

$$\frac{F_{\text{poly}}(R)}{k_{\text{B}}T} \simeq \frac{3\zeta}{2} \left( \frac{R^2}{2} + \frac{\beta\sigma_p}{V(R)} \right), \quad \beta \equiv N_p^2 \tau v A_{\text{surf}} R_0^2 / 3\zeta \quad (19)$$

where  $\beta \approx 37,200$  nm<sup>7</sup> is a constant for all simulated systems, since  $A_{\text{surf}} = 201$  nm<sup>2</sup> for all geometries, and because we use  $\tau = 1 = \zeta/2$  for PEG at the investigated temperature. Scaling behaviors are of course unaffected by the choice of numerical coefficients such as  $\tau$ ,  $v$ ,  $R_0^2/N_p$ , or  $\zeta$ . Minimizing  $F_{\text{poly}}$  with respect to  $R$  yields an equation  $RV^2(R) = \beta\sigma_p V'(R)$  for the equilibrium extension  $R_{\text{eq}}$  of the brush. For the special case of  $V(R) = \alpha R^\mu$  the solution is

$$R_{\text{eq}} = \left( \frac{\beta\sigma_p\mu}{\alpha} \right)^{1/(2+\mu)} \quad (20)$$

As we discussed,  $\mu \in [1, 3]$  for our systems, depending on the magnitude of  $R_{\text{eq}}$  with respect to NP dimensions, and the numerical factor  $\alpha$  can be read off from the analytical expressions for the volumes for each of the geometries. For  $\mu = 1$ ,  $\alpha = A_{\text{surf}}$ ; for  $\mu = 2$  the  $\alpha$ 's correspond to  $\sqrt{A_{\text{surf}}}$  times the numerical factors mentioned in Eqs. 12 and 16, and for  $\mu = 3$ ,  $\alpha = 4\pi/3$ . That is,  $\alpha \simeq A_{\text{surf}}^{(3-\mu)/2}$  and Eq. 20 simplifies to

$$R_{\text{eq}} \simeq \left( \frac{\beta\sigma_p\mu}{A_{\text{surf}}^{(3-\mu)/2}} \right)^{1/(2+\mu)} \quad (21)$$

Because we fixed  $A_{\text{surf}}$  and  $\beta$  in our simulations, we can use this formula supplemented by the mentioned numerical prefactors to roughly estimate the brush height for the different

shapes as function of  $\sigma_p$ . In addition, it can be used to predict the brush height and size of the PEGylated NP for systems with arbitrary  $N_p$ ,  $A_{\text{surf}}$ ,  $V$ , and shape characterized by  $\mu$  and numerical prefactor. In a more accurate numerical implementation, one instead minimizes Eq. 19 directly to obtain  $R_{\text{eq}}$ . Upon inserting  $R_{\text{eq}}$  into  $F$  we obtain the equilibrium free energy per chain

$$\frac{F_{\text{poly}}^{\text{eq}}}{k_{\text{B}}T} = \frac{3(2 + \mu)\beta\zeta\sigma_p}{2R_0^2V(R_{\text{eq}})} = \frac{3(2 + \mu)\beta\sigma_p}{\alpha R_0^2} \left( \frac{\beta\sigma_p\mu}{\alpha} \right)^{-\mu/(2+\mu)} \quad (22)$$

Using this expression, we can read off the scaling behavior of the equilibrium free energy of a single chain under good solvent conditions

$$\frac{F_{\text{poly}}^{\text{eq}}}{k_{\text{B}}T} \sim \sigma_p^{2/(2+\mu)} A_{\text{surf}}^{(\mu-1)/(2+\mu)} N^{(4-\mu)/(2+\mu)} \quad (23)$$

since  $V(R_{\text{eq}}) = \alpha R_{\text{eq}}^\mu$ , and where we highlighted the effect of grafting density  $\sigma_p$ , total surface area  $A_{\text{surf}}$ , and chain length,  $N_p$  on the equilibrium free energy. The total free energy of the PEGylated NOP is a factor  $\sigma_p A_{\text{surf}}$  larger, and it scales with  $\sigma_p$  as  $\sigma_p^{5/3}$  ( $\mu = 1$ ),  $\sigma_p^{3/2}$  ( $\mu = 2$ ), and  $\sigma_p^{7/5}$  ( $\mu = 3$ ). Similarly, we can discuss the scaling behavior of  $R_{\text{eq}}$  or  $\phi_0^{\text{eq}} = \phi_0(R_{\text{eq}})$ . For a quantitative comparison between Flory theory and our simulation results before endocytosis we use  $\tau = w = 1$ , and find the minimum of  $F_{\text{poly}}$  numerically using the complete expressions for the coated volumes  $V(R)$  of the various geometries given in Eqs. 8, 9, 14, and 15. The scaling results in Eqs. 22 and 23 just serve to highlight on how to obtain qualitative behavior via the Flory route.

The free energies for both configurations, before and after endocytosis, we calculate starting from an SCF expression, as described in our previous study [10], using the surface normals to calculate  $\langle r^2 \rangle$  for the estimation of  $F_{\text{el}}$ , while  $F_{\text{int}}$  is directly obtained from the recorded volume fraction profile on a grid. In contrast to the SCF approach, the above-mentioned Flory approach cannot be used to calculate free energies after endocytosis because the Flory approach implicitly assumes a constant volume fraction profile. The observed large inhomogeneities, and stretch of selected polymers that are bound to receptors, would falsify this approach. Still, an increase of the Flory free energy is expected due to the overall decrease of available volume after endocytosis.

#### 4. Internalization pathway of PEGylated nanoparticles (NPs)

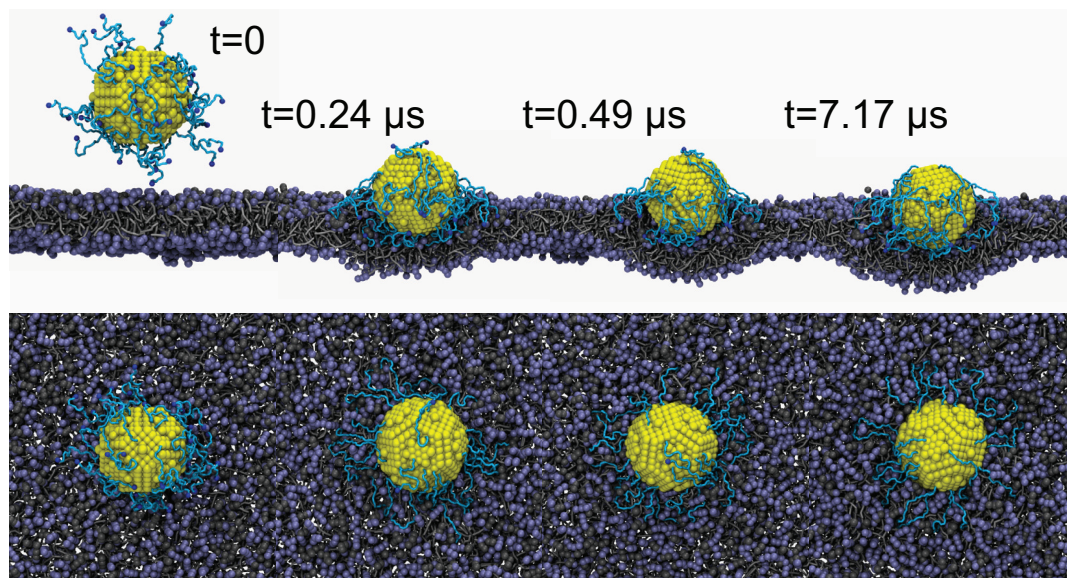


**Figure S5.** Representative DPD simulation snapshots at specified times for the internalization process of PEGylated spherical NP with grafting density  $\sigma_p = 0.2$  chains/nm<sup>2</sup>. The core of PEGylated NP is colored by yellow. The grafted PEG chains are colored by cyan. The lipid heads and tails are represented by iceblue beads and silver lines, respectively. The targeting moieties conjugated on the free ends of grafted chains are colored by blue. Gray beads on the lipid heads denote the receptor, which have attractive interactions with targeting moieties with strength  $\epsilon_b = 7.65k_B T$ .

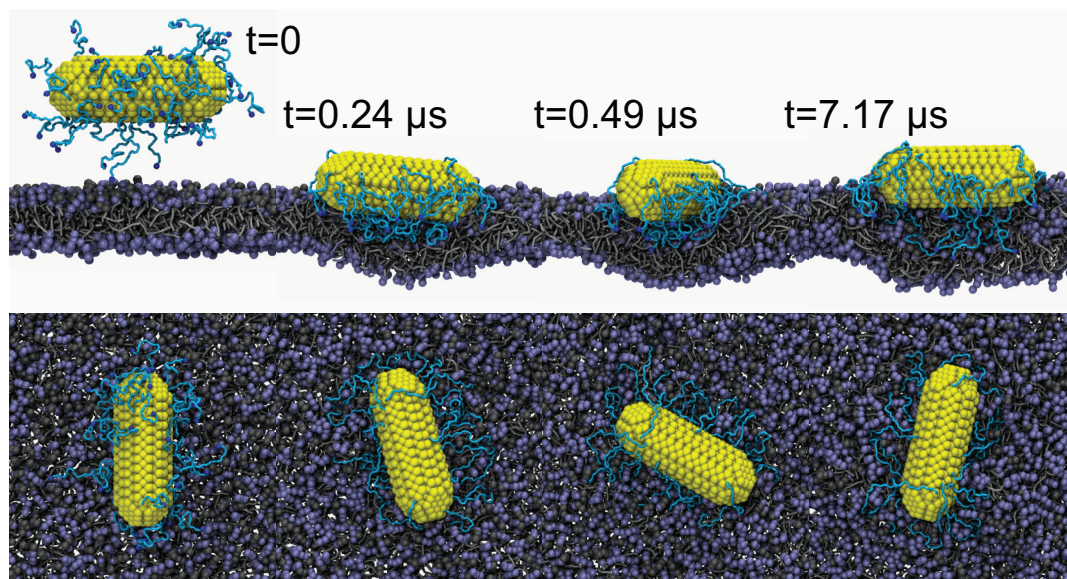


**Figure S6.** Same as Fig. S5 for the rod-like NP (again for  $\sigma_p = 0.2$  chains/nm<sup>2</sup>).

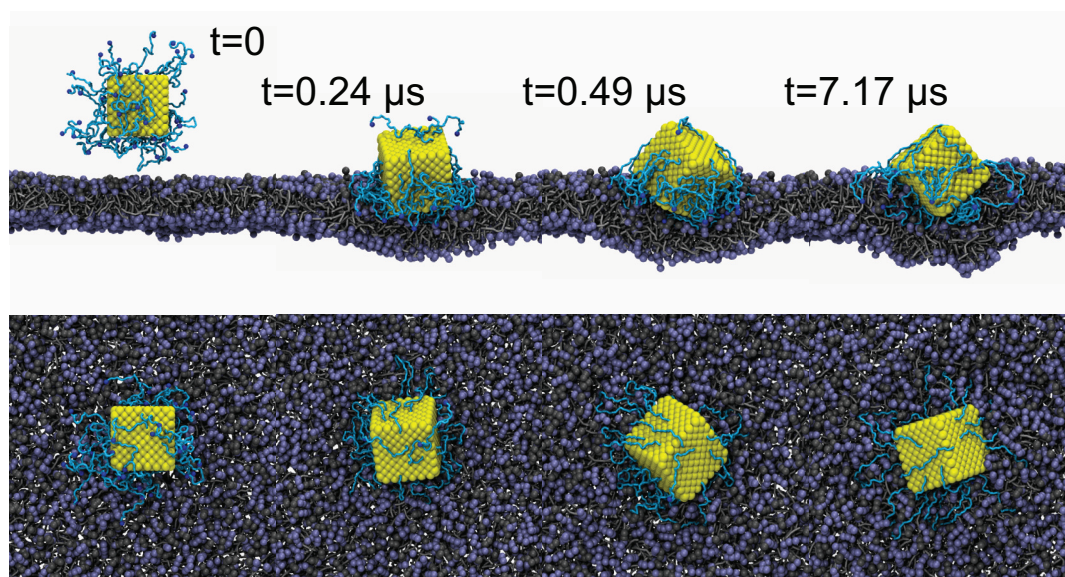


**Figure S7.** Same as Fig. S5 for the cubic NP (again for  $\sigma_p = 0.2$  chains/nm<sup>2</sup>).

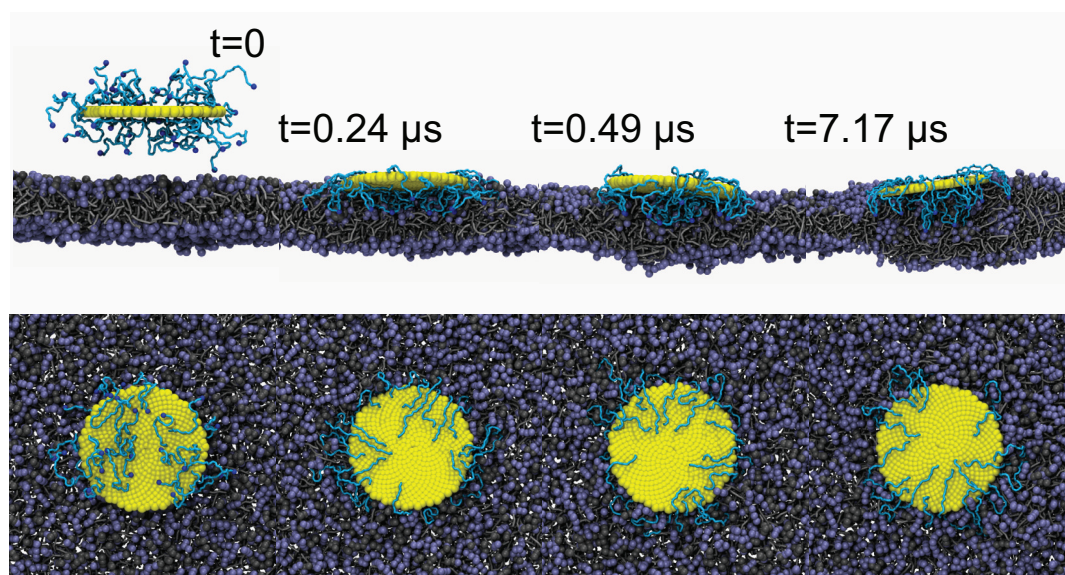


**Figure S8.** Same as Fig. S5 for the disk-like NP (again for  $\sigma_p = 0.2$  chains/nm<sup>2</sup>).

## 5. Volume fraction distributions of PEG monomers

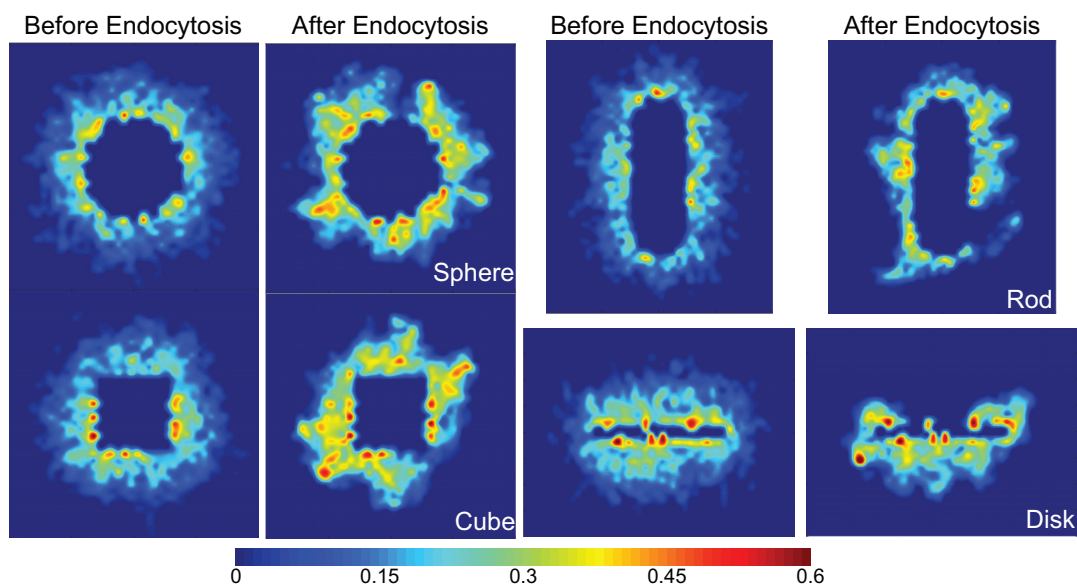


**Figure S9.** Cross-sectional views on the PEG volume fraction profiles  $\phi(\mathbf{r})$  of differently shaped NPs with grafting density  $\sigma_p = 0.6$  chains/nm<sup>2</sup> before and after endocytosis. Note that the rod- and disk-like NPs are not fully internalized.

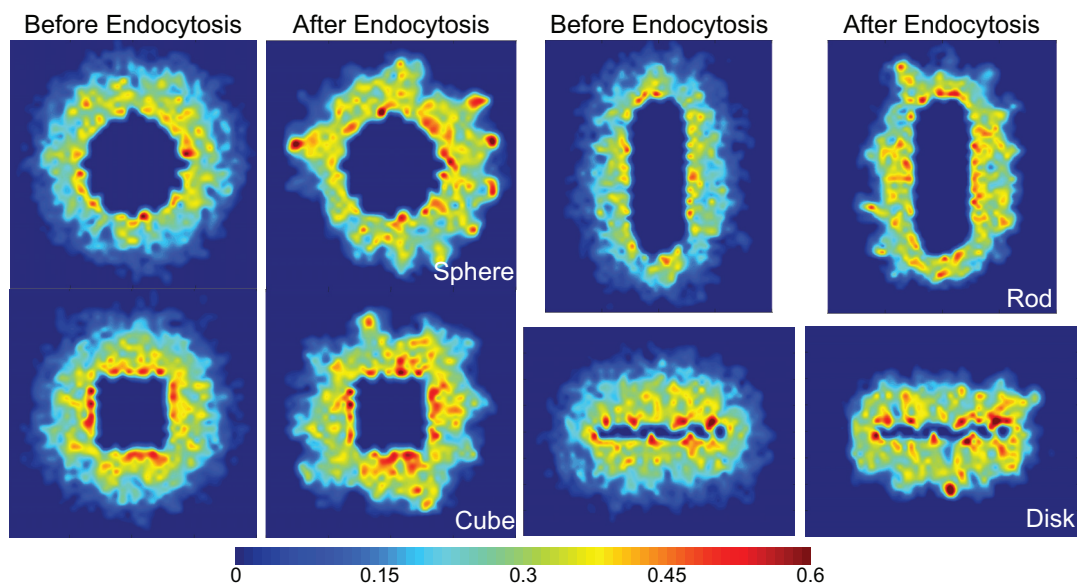


**Figure S10.** Cross-sectional views on the PEG volume fraction profiles  $\phi(\mathbf{r})$  of differently shaped NPs with grafting density  $\sigma_p = 1.2$  chains/nm<sup>2</sup> before and after endocytosis.

## 6. Entry angle effect during endocytosis of PEGylated rod- and disk-like NPs

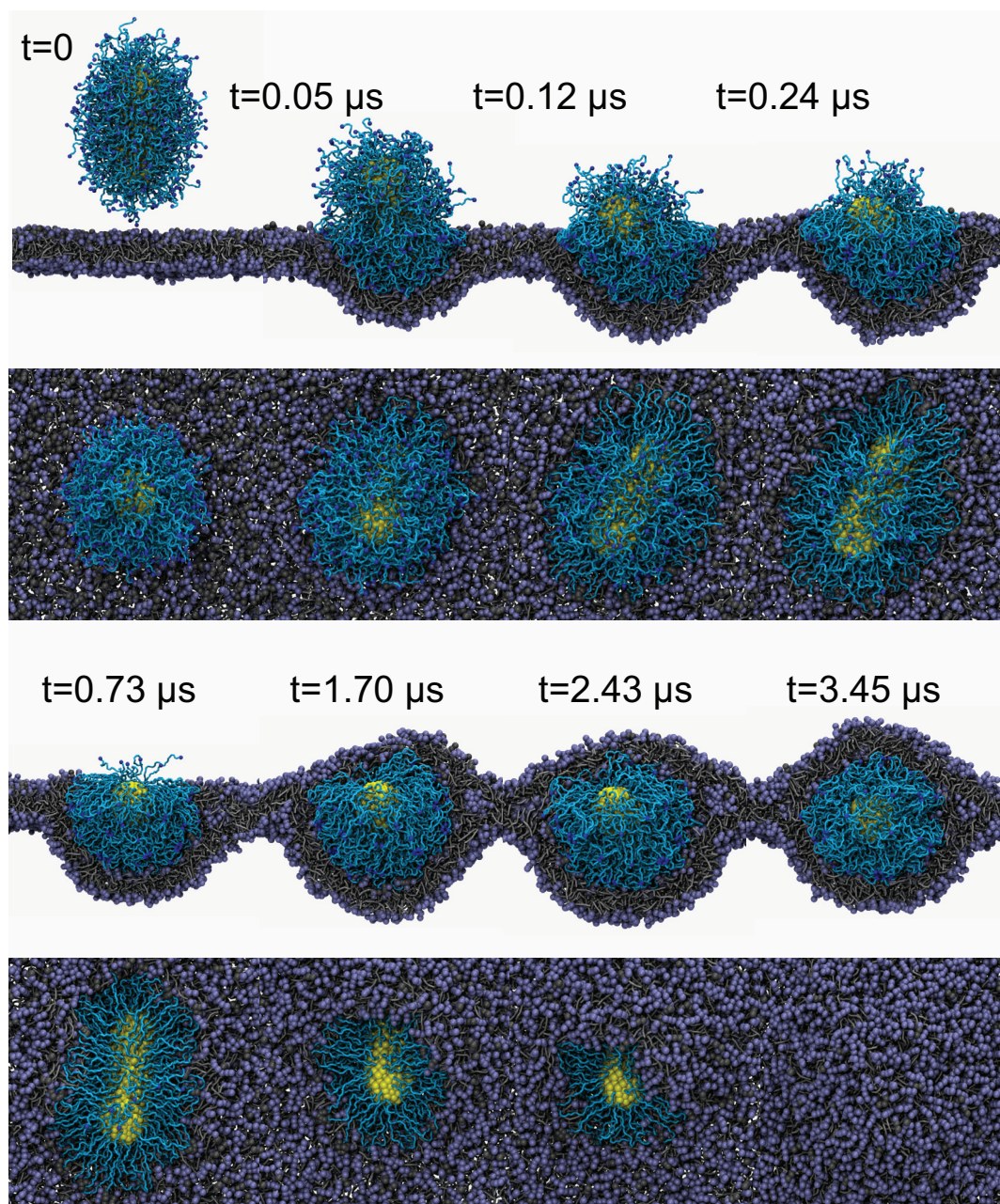


**Figure S11.** Representative DPD simulation snapshots at specified times  $t$  for the internalization process of the PEGylated rod-like NP with grafting density  $\sigma_p = 1.6$  chains/nm<sup>2</sup> and vertical docking position (shown from two different view points). The core of PEGylated NP is colored by yellow. The grafted PEG chains are colored by cyan. The lipid heads and tails are represented by iceblue beads and silver lines, respectively. The targeting moieties conjugated on the free ends of grafted chains are colored by blue. Gray beads on the lipid heads denote the receptor, which have attractive interactions with targeting moieties with strength  $\epsilon_b = 7.65k_B T$ .

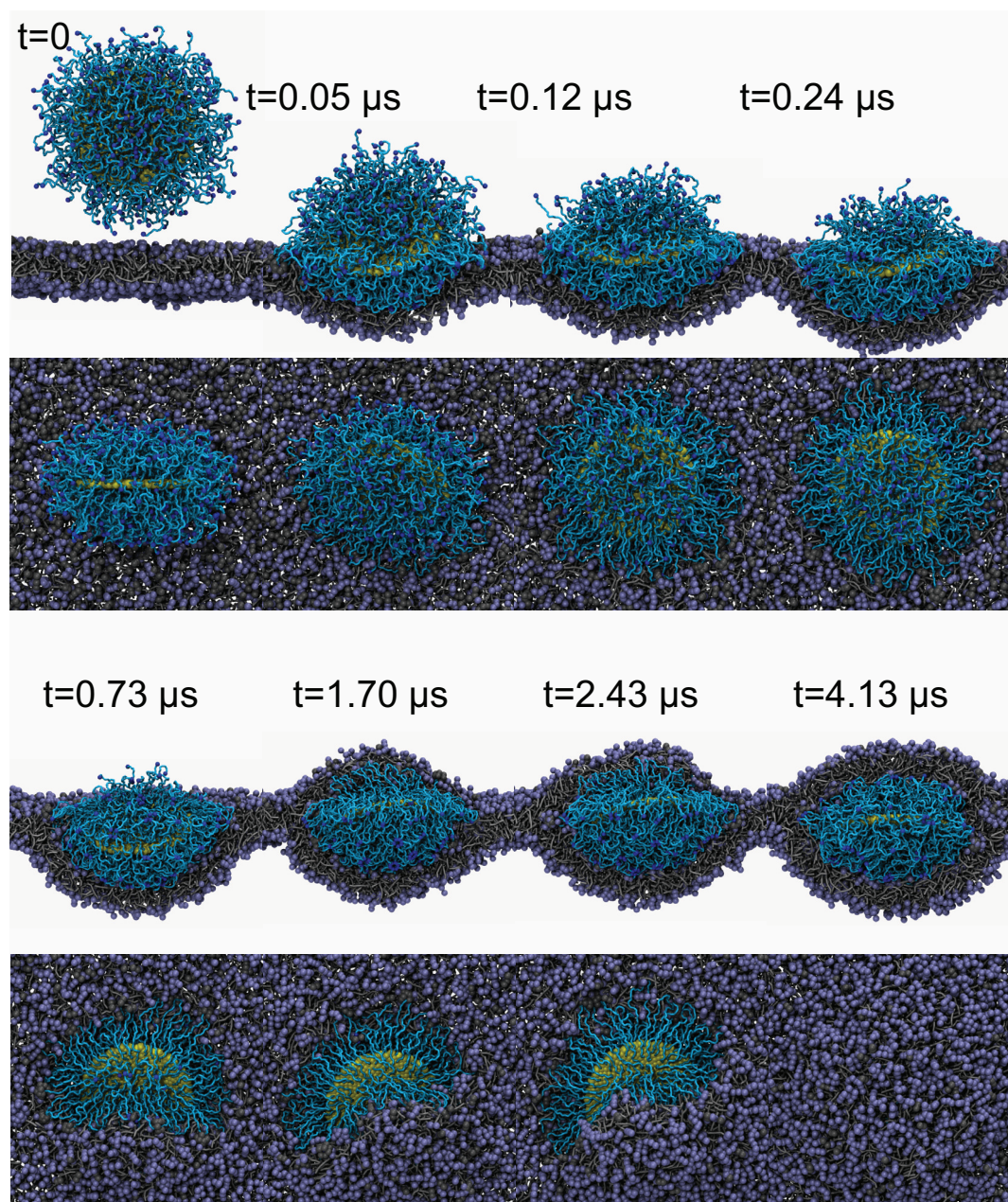


**Figure S12.** Same as preceding Fig. S11 now for the disk-like NP in vertical docking position (again for  $\sigma_p = 1.6$  chains/nm<sup>2</sup>).

## 7. Elastic bending energy of membrane

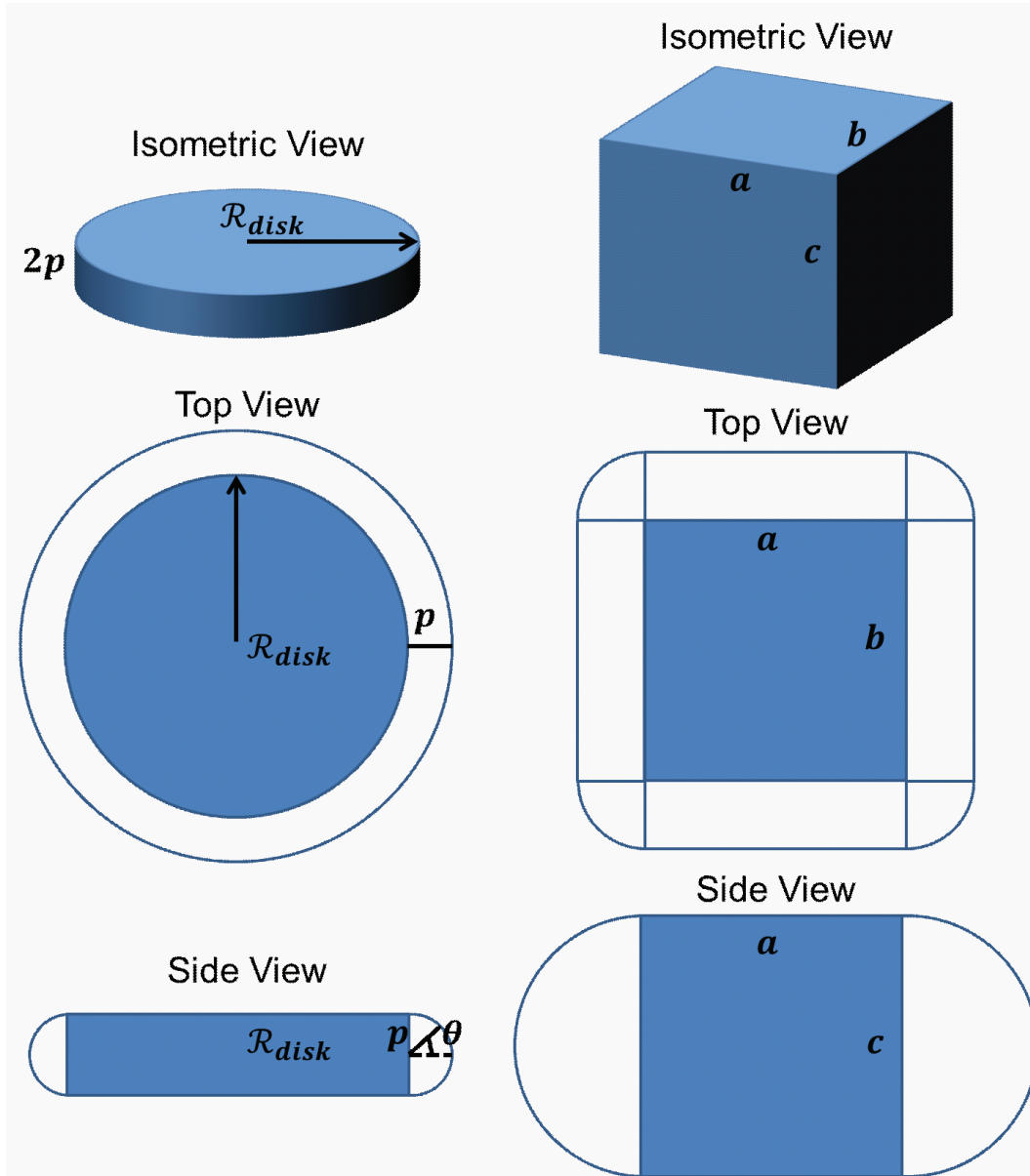


**Figure S13.** Disk-like (left column) and cuboidal (right column) NPs. The particles are colored by blue. The endosome shapes are given by the blue outline.

The elastic bending energy associated with the deformation of the membrane during endocytosis can be determined by the Helfrich-Canham-Evans free energy [16–18],

$$\Delta F_{\text{memb}} = \int \left[ \frac{1}{2} \kappa (c_1 + c_2 - c_s)^2 + \bar{\kappa} c_1 c_2 \right] dA, \quad (24)$$

where  $\kappa$  and  $\bar{\kappa}$  are the curvature and saddle-splay moduli of the membrane, respectively;  $c_1$  and  $c_2$  are the two principle curvatures of the final vesicle shape, and  $c_s$  is the spontaneous curvature. The product  $c_1 c_2$  is the Gaussian curvature, which usually can be ignored for

a homogeneous lipid bilayer [16, 19]. Considering the sizes of NPs in this study, the spontaneous curvature is rather small [20], assuming  $c_s = 0$ , the above equation further reduces to

$$\Delta F_{\text{memb}} = \int \frac{1}{2} \kappa (c_1 + c_2)^2 dA, \quad (25)$$

Integrating Eq. 25 over the surface area of the endosome shape (membrane wrapped around the PEGylated NP) renders the elastic bending energy of the membrane. For a spherical NP with radius  $\mathcal{R}_{\text{sphere}}$ , the two principle curvatures are constant and  $c_1 = c_2 = 1/\mathcal{R}_{\text{sphere}}$ , thus the elastic bending energy can be analytically obtained as

$$\Delta F_{\text{memb}}^{\text{sphere}} = 8\pi\kappa. \quad (26)$$

For a rod-like NP with two hemispherical caps of radius  $\mathcal{R}_{\text{rod}}$ , and a cylinder with length  $\mathcal{L}_{\text{rod}}$  joining them, Eq. 25 can also be analytically solved by splitting the integration into parts (the spherical caps and the cylindrical surface), gives

$$\Delta F_{\text{memb}}^{\text{rod}} = 8\pi\kappa + \pi\kappa\mathcal{L}_{\text{rod}}/\mathcal{R}_{\text{rod}}, \quad (27)$$

since the two principle curvatures for a cylinder are  $c_1 = 1/\mathcal{R}_{\text{rod}}$  and  $c_2 = 0$ . For a cuboid with length  $a$ , width  $b$  and height  $c$ , the endosomal surface reduces to a single sphere with radius  $c/2$ , a cylinder of radius  $c/2$  and length  $b$ , another cylinder of radius  $b/2$  and length  $a$ , and two rectangles with zero curvature, as denoted in Fig. S13. Thus, Eq. 25 can be rewritten as,

$$\Delta F_{\text{memb}}^{\text{cuboid}} = \int \frac{1}{2} \kappa \left(\frac{2}{c}\right)^2 dA + \int \frac{1}{2} \kappa \left(\frac{4}{c}\right)^2 dA = \left[ \frac{2(a+b)}{c} + 8 \right] \pi\kappa, \quad (28)$$

where we could evaluate the integrals analytically. For a cubic NP with side length  $\mathcal{L}_{\text{cube}}$ , we have  $a = b = c = \mathcal{L}_{\text{cube}}$ , thus

$$\Delta F_{\text{memb}}^{\text{cube}} = 12\pi\kappa. \quad (29)$$

For a disk-like NP, the vesicle shape is assumed to be the outer half of a torus with wheel radius  $\mathcal{R}_{\text{disk}}$  and tube radius  $p$  along with two circular, zero curvature, areas of  $\pi\mathcal{R}_{\text{disk}}^2$  for each. Thus, according to Eq. 25, the elastic bending energy is

$$\Delta F_{\text{memb}}^{\text{disk}} = \pi\kappa \int_{-\pi/2}^{\pi/2} \left[ \frac{\mathcal{R}_{\text{disk}} + 2p \cos \theta}{2p(\mathcal{R}_{\text{disk}} + p \cos \theta)} \right]^2 p(\mathcal{R}_{\text{disk}} + p \cos \theta) d\theta, \quad (30)$$

where  $p(\mathcal{R}_{\text{disk}} + p \cos \theta)$  is the Jacobian for the half torus and  $\theta$  is integrated from  $-\pi/2$  to  $\pi/2$ . Then, we have

$$\Delta F_{\text{memb}}^{\text{disk}} = \left[ 2 + \frac{\mathcal{R}_{\text{disk}}^2 \arctan \sqrt{\frac{\mathcal{R}_{\text{disk}} - p}{\mathcal{R}_{\text{disk}} + p}}}{p\sqrt{\mathcal{R}_{\text{disk}}^2 - p^2}} \right] \pi\kappa. \quad (31)$$

Here the thickness of the PEGylated disk is rather small and about 0.344 nm, thus  $p = 0.172$  nm (half of the thickness). Considering  $\mathcal{R}_{\text{disk}} = 5.66$  nm, we have  $\Delta F_{\text{memb}}^{\text{disk}} = 27.33\pi\kappa$ .

## 8. PEGylated Star-shaped NP

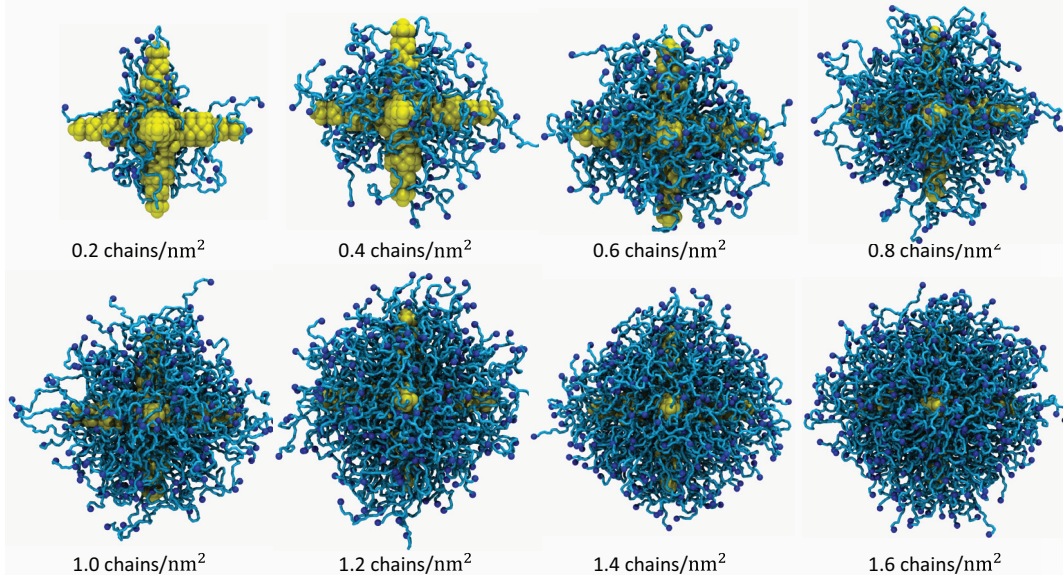


**Figure S14.** Same as Fig. S1 for the star-shaped NP.

In recent years, the gold star-shaped NPs have been recognized as a promising drug carrier [21–23]. However, the atomistic structure of the gold nanostar is still not well-defined, as it may have different branches and these branches have different lengths and diameters [24]. Here we adopt a simplified model to represent the star-shaped NP. A simple star for which volume and area is immediately known exactly is one that builds onto a regular convex polyhedron, a so-called Platonic body. Let us consider here the case where the Platonic body is a cube, corresponding to a star with 6 arms. Denote with  $2\mathcal{R}_{\text{star}}$  the side length of the centered cube and with  $\mathcal{L}_{\text{star}}$  the heights of the identical paraboloids with their identical circular bases of radii  $\mathcal{R}_{\text{star}}$  built onto any one of the 6 faces. With the volume  $v_1$  and surface area  $a_1$  of a single paraboloid,

$$v_1 = \frac{1}{2}\pi\mathcal{R}_{\text{star}}^2\mathcal{L}_{\text{star}} \quad (32)$$

$$a_1 = \frac{\pi\mathcal{R}_{\text{star}}}{6\mathcal{L}_{\text{star}}^2}[(\mathcal{R}_{\text{star}}^2 + 4\mathcal{L}_{\text{star}}^2)^{3/2} - \mathcal{R}_{\text{star}}^3] \quad (33)$$

Thus, the volume and surface area of the regular 6-arms star is

$$v_6 = (2\mathcal{R}_{\text{star}})^3 + 6v_1 \quad (34)$$

$$A_{\mathcal{R},\mathcal{L}}^{\text{star}} = 6[a_1 + (2\mathcal{R})^2 - \pi\mathcal{R}^2] \quad (35)$$

If for example,  $\mathcal{L}_{\text{star}}$  is some multiple of  $\mathcal{R}_{\text{star}}$ , say

$$\mathcal{L}_{\text{star}} = c\mathcal{R}_{\text{star}}, \quad (36)$$

then the above expressions simplify to

$$v_6 = \mathcal{R}_{\text{star}}^3(8 + 3\pi c) \quad (37)$$

$$A_{\mathcal{R},\mathcal{L}}^{\text{star}} = \left\{ 24 - 6\pi + \frac{\pi}{c^2} [(1 + 4c^2)^{3/2} - 1] \right\} \mathcal{R}^2, \quad c = \frac{\mathcal{L}}{\mathcal{R}} \quad (38)$$

To satisfy the total surface area  $A = 201 \text{ nm}^2$ , we set  $c = 4$  and  $\mathcal{R}_{\text{star}} = 1.365 \text{ nm}$ , implying  $\mathcal{L}_{\text{star}} = 5.46 \text{ nm}$ . The set of these parameters is within the experimental observed gold nanostars [24]. The PEG volume of such a 6-arms star at coating thickness  $R$  is approximately given by

$$V_{\mathcal{R},\mathcal{L}}^{\text{star}}(R) \approx V_{2\mathcal{R}}^{\text{cube}}(R) + 3\pi R(2\mathcal{R} + R)\mathcal{L} \quad (39)$$

Here we also briefly mention how the above star-shaped NP can be constructed in our molecular simulations. Given some regular grid with nodes at  $(x, y, z)$ , a node resides inside the star if  $\max(|x|, |y|, |z|) \leq a$ , or  $|z| \geq a$  and  $x^2 + y^2 \leq a^2 [1 - (|z| - a)/h]$ , or  $|x| \geq a$  and  $y^2 + z^2 \leq a^2 [1 - (|x| - a)/h]$ , or  $|y| \geq a$  and  $z^2 + x^2 \leq a^2 [1 - (|y| - a)/h]$ . The molecular model of PEGylated star-shaped NPs is given in Fig. S14. The typical snapshots for internalization of PEGylated star-shaped NPs are presented in Figs. S15-S16.

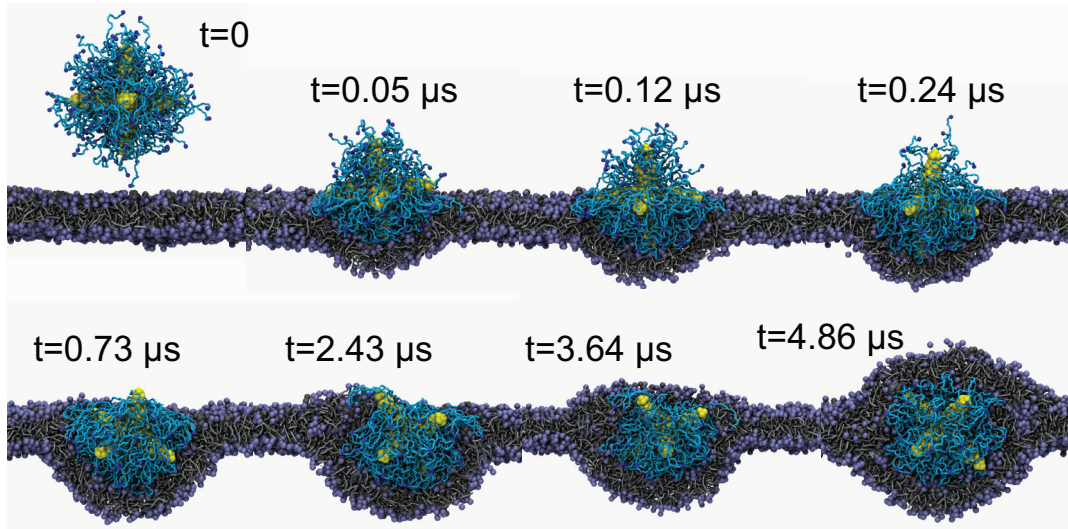


**Figure S15.** Representative DPD simulation snapshots at specified times for the internalization process of PEGylated star-shaped NP with grafting density  $\sigma_p = 0.8 \text{ chains/nm}^2$ . The core of PEGylated NP is colored by yellow. The grafted PEG chains are colored by cyan. The lipid heads and tails are represented by iceblue beads and silver lines, respectively. The targeting moieties conjugated on the free ends of grafted chains are colored by blue. Gray beads on the lipid heads denote the receptor, which have attractive interactions with targeting moieties with strength  $\epsilon_b = 7.65k_B T$ .

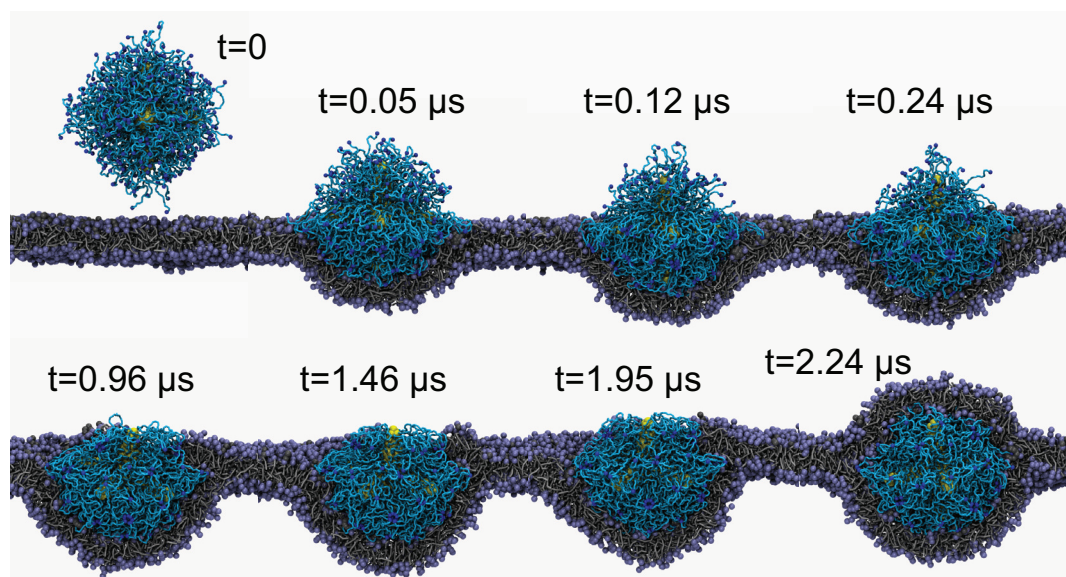


**Figure S16.** Same as Fig. S15 for the star-shaped NP (again for  $\sigma_p = 1.6$  chains/nm<sup>2</sup>).

## References

- [1] PJ Hoogerbrugge and JMVA Koelman. Simulating microscopic hydrodynamic phenomena with dissipative particle dynamics. *EPL (Europhysics Letters)*, 19(3):155, 1992.
- [2] Pep Espanol and Patrick Warren. Statistical mechanics of dissipative particle dynamics. *EPL (Europhysics Letters)*, 30(4):191, 1995.
- [3] Robert D Groot and Patrick B Warren. Dissipative particle dynamics: bridging the gap between atomistic and mesoscopic simulation. *J. Chem. Phys.*, 107(11):4423, 1997.
- [4] RD Groot and KL Rabone. Mesoscopic simulation of cell membrane damage, morphology change and rupture by nonionic surfactants. *Biophys. J.*, 81(2):725–736, 2001.
- [5] Yinfeng Li, Xuejin Li, Zhonghua Li, and Huajian Gao. Surface-structure-regulated penetration of nanoparticles across a cell membrane. *Nanoscale*, 4(12):3768–3775, 2012.
- [6] Yinfeng Li, Hongyan Yuan, Annette von dem Bussche, Megan Creighton, Robert H Hurt, Agnes B Kane, and Huajian Gao. Graphene microsheets enter cells through spontaneous membrane penetration at edge asperities and corner sites. *Proc. Natl. Acad. Sci. U.S.A.*, 110(30):12295–12300, 2013.
- [7] Julian C Shillcock and Reinhard Lipowsky. Tension-induced fusion of bilayer membranes and vesicles. *Nat. Mater.*, 4(3):225–228, 2005.
- [8] Hwankyu Lee, Alex H de Vries, Siewert-Jan Marrink, and Richard W Pastor. A coarse-grained model for polyethylene oxide and polyethylene glycol: conformation and hydrodynamics. *J. Phys. Chem. B*, 113(40):13186–13194, 2009.
- [9] Susumu Saeki, Nobuhiro Kuwahara, Mitsuo Nakata, and Motozo Kaneko. Upper and lower critical solution temperatures in poly (ethylene glycol) solutions. *Polymer*, 17(8):685–689, 1976.
- [10] Y. Li, M. Kröger, and W. K. Liu. Endocytosis of pegylated nanoparticles accompanied by structural and free energy changes of the grafted polyethylene glycol. *Biomaterials*, 35(30):8467–8478, 2014.
- [11] I. Szleifer. Statistical thermodynamics of polymers near surfaces. *Curr. Opin. Colloid Interface Sci.*, 1(3):416–423, 1996.
- [12] I. Szleifer. Protein adsorption on surfaces with grafted polymers: a theoretical approach. *Biophys. J.*, 72(2):595–612, 1997.
- [13] I. Szleifer and M. A. Carignano. Tethered polymer layers: phase transitions and reduction of protein adsorption. *Macromol. Rapid Commun.*, 21(8):423–448, 2000.
- [14] J. M. H. M. Scheutjens and G. J. Fleer. Statistical theory of the adsorption of interacting chain molecules. 1. partition function, segment density distribution, and adsorption isotherms. *J. Phys. Chem.*, 83(12):1619–1635, 1979.
- [15] C. M. Wijmans, J. M. H. M. Scheutjens, and E. B. Zhulina. Self-consistent field theories for polymer brushes: lattice calculations and an asymptotic analytical description. *Macromolecules*, 25(10):2657–2665, 1992.
- [16] U. Seifert. Configurations of fluid membranes and vesicles. *Adv. Phys.*, 46(1):13–137, 1997.
- [17] P. B. Canham. The minimum energy of bending as a possible explanation of the biconcave shape of the human red blood cell. *J. Theor. Biol.*, 26(1):61–81, 1970.
- [18] W. Helfrich. Elastic properties of lipid bilayers: theory and possible experiments. *Z. Naturforsch. C*, 28(11):693, 1973.
- [19] S. L. Das, J. T. Jenkins, and T. Baumgart. Neck geometry and shape transitions in vesicles with co-existing fluid phases: Role of gaussian curvature stiffness vs. spontaneous curvature. *EPL (Europhysics Letters)*, 86(4):48003, 2009.
- [20] S. Leikin, M. M. Kozlov, N. L. Fuller, and R. P. Rand. Measured effects of diacylglycerol on structural and elastic properties of phospholipid membranes. *Biophys. J.*, 71(5):2623–2632, 1996.
- [21] Duncan Hieu M Dam, Kayla SB Culver, Irawati Kandela, Raymond C Lee, Kavita Chandra, Hyojin Lee, Christine Mantis, Andrey Ugolkov, Andrew P Mazar, and Teri W Odom. Biodistribution and in vivo toxicity of aptamer-loaded gold nanostars. *Nanomedicine: Nanotechnology, Biology and Medicine*, 11(3):671–679, 2015.
- [22] Duncan Hieu M Dam, Kayla SB Culver, and Teri W Odom. Grafting aptamers onto gold nanostars

- increases in vitro efficacy in a wide range of cancer cell types. *Molecular pharmaceutics*, 11(2):580–587, 2014.
- [23] Duncan Hieu M Dam, Kayla SB Culver, Patrick N Sisco, and Teri W Odom. Research spotlight: Shining light on nuclear-targeted therapy using gold nanostar constructs. *Therapeutic delivery*, 3(11):1263–1267, 2012.
- [24] Hsiangkuo Yuan, Christopher G Khoury, Hanjun Hwang, Christy M Wilson, Gerald A Grant, and Tuan Vo-Dinh. Gold nanostars: surfactant-free synthesis, 3d modelling, and two-photon photoluminescence imaging. *Nanotechnology*, 23(7):075102, 2012.